

All-dielectric active terahertz photonics driven by bound states in the continuum

Han, Song; Cong, Longqing; Srivastava, Yogesh Kumar; Qiang, Bo; Rybin, Mikhail V.; Kumar, Abhishek; Jain, Ravikumar; Lim, Wen Xiang; Achanta, Venu Gopal; Prabhu, Shriganesh S.; Wang, Qijie; Kivshar, Yuri S.; Singh, Ranjan

2019

Han, S., Cong, L., Srivastava, Y. K., Qiang, B., Rybin, M. V., Kumar, A., . . . Singh, R. (2019). All-dielectric active terahertz photonics driven by bound states in the continuum. *Advanced Materials*, 31(37), 1901921-. doi:10.1002/adma.201901921

<https://hdl.handle.net/10356/141634>

<https://doi.org/10.1002/adma.201901921>

This is the peer reviewed version of the following article: Han, S., Cong, L., Srivastava, Y. K., Qiang, B., Rybin, M. V., Kumar, A., . . . Singh, R. (2019). All-dielectric active terahertz photonics driven by bound states in the continuum. *Advanced Materials*, 31(37), 1901921-. doi:10.1002/adma.201901921, which has been published in final form at <https://doi.org/10.1002/adma.201901921>. This article may be used for non-commercial purposes in accordance with Wiley Terms and Conditions for Use of Self-Archived Versions.

DOI: 10.1002/((please add manuscript number))

Article type: full paper

All-dielectric active terahertz photonics driven by bound states in the continuum

Song Han^{1,2}, Longqing Cong^{1,2}, Yogesh Kumar Srivastava^{1,2}, Bo Qiang^{2,3}, Mikhail V. Rybin^{4,5}, Abhishek Kumar^{1,2}, Ravikumar Jain⁶, Wen Xiang Lim^{1,2}, Venu Gopal Achanta⁶, Shriganesh S. Prabhu⁶, Qijie Wang^{2,3}, Yuri S. Kivshar^{5,7}, and Ranjan Singh^{1,2}*

Song Han, Dr. Longqing Cong, Dr. Yogesh Kumar Srivastava, Abhishek Kumar, Dr. Wen Xiang Lim, and Prof. Ranjan Singh

Division of Physics and Applied Physics, School of Physical and Mathematical Sciences, Nanyang Technological University, Singapore 637371, Singapore

Song Han, Dr. Longqing Cong, Dr. Yogesh Kumar Srivastava, Bo Qiang, Abhishek Kumar, Dr. Wen Xiang Lim, Prof. Qijie Wang, and Prof. Ranjan Singh

Centre for Disruptive Photonic Technologies, The Photonics Institute, Nanyang Technological University, Singapore 639798, Singapore

E-mail: ranjans@ntu.edu.sg

Bo Qiang and Prof. Qijie Wang

Centre for OptoElectronics and Biophotonics, School of Electrical and Electronic Engineering and The Photonics Institute, Nanyang Technological University, Singapore 639798, Singapore

Dr. Mikhail V. Rybin

Ioffe Institute, St Petersburg 194021, Russia

Dr. Mikhail V. Rybin and Prof. Yuri S. Kivshar

ITMO University, St Petersburg 197101, Russia

Prof. Yuri S. Kivshar

Nonlinear Physics Center, Australian National University, Canberra ACT 2601, Australia

Ravikumar Jain, Prof. Venu Gopal Achanta, and Prof. Shriganesh S. Prabhu

Department of Condensed Matter Physics and Material Science, Tata Institute of Fundamental Research, Mumbai 400005, India

Keywords: Terahertz; All-dielectric metasurface; Bound states in the continuum; Optically active metadevices; Ultrafast switching

Abstract

Remarkable emergence of all-dielectric meta-photonics governed by the physics of high-index dielectric materials offer a low-loss platform for an efficient manipulation and subwavelength control of electromagnetic waves from microwaves to visible frequencies. Dielectric metasurfaces can focus electromagnetic waves, generate structured beams and vortices, enhance local fields for advanced sensing and provide novel functionalities for classical and quantum technologies. Recent advances in meta-photonics are associated with the exploration of **exotic electromagnetic modes** called the *bound states in the continuum* (BICs), which offer a simple interference mechanism to achieve large quality factors (Q) through excitation of *supercavity modes* in dielectric nanostructures and resonant metasurfaces. Here, we experimentally demonstrate a BIC driven terahertz metasurface with dynamic control of high- Q silicon supercavities that are reconfigurable at nanosecond timescale. We reveal that such supercavities enable low-power, optical induced terahertz switching and modulation of sharp resonances for potential applications in lasing, mode multiplexing, and biosensing.

1
2
3
4 Dielectric cylinder resonators were theoretically proposed by Richtmyer in 1939 [1]. Since then,
5
6 dielectric resonator antennas have been extensively investigated at microwave frequencies [2-7].
7
8 In 2002, O' Brien and Pendry investigated a composite structure consisting of high-index dielectric
9
10 cylinders that was theoretically shown to possess effective negative permeability [8]. This
11
12 approach became essential for constructing negative index media which laid the strong foundation
13
14 for the burgeoning field of metamaterial photonics. Split-ring resonators as the basic building
15
16 blocks of metamaterials were first proposed to be made up of metallic inclusions at the microwave
17
18 frequencies [9]. However, beyond the microwave frequencies, metals show considerable Ohmic
19
20 loss which created the need for all-dielectric resonator platform with the promise to offer low-loss
21
22 meta-optics and photonics. The last few years have witnessed an unprecedented use of dielectrics
23
24 in optical metamaterials based on high-index dielectric materials that have strongly emerged as an
25
26 alternative approach to disrupt the lossy metal-based subwavelength photonics [10-18].
27
28
29
30
31
32

33
34 Several interesting phenomena of metamaterials are driven by strong resonances, and their quality
35
36 (Q) factors become an extremely important parameter that determines the strength of light-matter
37
38 interaction. The structures with high- Q factors offer a new route for strong localization of
39
40 electromagnetic energy in near fields that allow ultrasensitive sensors and other optical devices
41
42 [19-23]. Recent trends in this field are based on so-called *bound states in the continuum* (BICs)
43
44 for achieving extremely high- Q resonances in nanoparticles and metasurfaces for the realization
45
46 of many useful functionalities including lasing and biosensing [24-28]. The BICs originated from
47
48 quantum mechanics. However, the phenomenon was later rediscovered as an important physical
49
50 concept of destructive interference in other fields of wave physics, including optics. **Theoretically,**
51
52 **BICs show infinite Q factors. However, in practical devices, BIC can be realized as a quasi-BIC**
53
54 **in the form of a supercavity mode when both Q factor and resonance linewidth become finite at**
55
56
57
58
59
60
61
62
63
64
65

1
2
3
4 the BIC conditions due to material's absorption and other perturbations. Importantly, the BIC-
5
6 inspired mechanism of light localization makes it possible to realize high- Q resonances in
7
8 metasurfaces that can be designed as pixelated dielectric metasurfaces for imaging-based
9
10 molecular barcoding [28].
11
12

13
14 Here, we employ the physics of BICs for achieving high- Q factors in terahertz dielectric
15
16 metasurfaces and realize an all-dielectric, active supercavity that can be dynamically switched at
17
18 an ultrafast timescale. We employ terahertz (THz) metasurfaces made up of silicon that offers
19
20 optically tunable THz conductivity upon excitation by short optical pulses. The optical pump with
21
22 photon energy larger than the semiconductor bandgap creates free charge carriers in the
23
24 semiconducting material [30, 31]. Optical pump–THz probe studies in a variety of semiconductors
25
26 revealed free-carrier-induced changes in complex conductivity described by the Drude model [32-
27
28 34]. The recombination dynamics of the photo-generated carriers could be tailored at ultrafast
29
30 timescale. As a result, the photoconductivity of semiconductors provide a unique approach for the
31
32 dynamic control of high- Q THz resonances by tuning the external photo-excitation pump fluence.
33
34 This approach opens broad perspectives for designing active metamaterials and photonic devices
35
36 towards filling the THz gap.
37
38
39
40
41
42

43 44 RESULTS

45
46 **Bound states in the continuum and supercavity modes.** In photonics, the non-radiative
47
48 eigenmodes of a periodic membrane that lie below the light cone are referred as guided modes
49
50 [35]. In contrast to these guided modes, modes located above the light cone generally couple to
51
52 radiation continuum of free space. However, there exist modes above the light cone that are
53
54 uncoupled from the free space and are known as the BICs [24-26]. The existing body of literature
55
56 distinguishes several mechanisms of BICs. The first one is *symmetry-protected BICs* [24, 36, 37].
57
58
59
60
61

1
2
3
4 The simplest case of BICs is related to the Γ point in the first Brillouin zone, while the symmetry
5
6 may also lead to BIC at other high symmetry points [38]. The intuitive physical description of the
7
8 symmetry-protected BICs at the Γ point is that odd modes are uncoupled from the free space plane
9
10 waves propagating in the normal direction. However, the rigorous symmetry analysis involves less
11
12 intuitive methods of the group theory (see Supplemental Materials). The second possibility is to
13
14 form BICs at an *off- Γ point in photonic crystal membrane* due to destructive interference between
15
16 the leaky tails of two modes [24, 25, 39, 40]. This effect can be described almost analytically by
17
18 account of expansion over a small number of plane waves. The third mechanism describes a
19
20 *resonance-trapped BICs in metasurfaces* reported recently [26, 41, 42]. It also occurs due to the
21
22 destructive interference between tails of leaky modes, while we distinguish this mechanism since
23
24 effects in photonic crystals and metamaterials have different descriptions [43]. We recall that
25
26 metasurfaces consist of resonant structural elements, which are responsible for the unusual
27
28 properties of these structures. Unlike the photonic crystal membranes, the metasurfaces require a
29
30 large number of plane waves to reproduce a multipole resonance in the structural element correctly,
31
32 which correspond to almost flat dispersion-less branch at the Γ point [44].
33
34
35
36
37
38
39
40

41 Although BICs are uncoupled to the free space, they are discrete states in the continuum of leaky
42
43 modes. Thus, a small variation of parameters turns BICs into a leaky mode with extremely high-
44
45 Q factor, which is known as supercavity mode [29]. Moreover, the true BICs occur only in
46
47 infinitely elongated systems [25], thus in most practical devices, all possible BICs turn to
48
49 supercavity modes with high- Q factors. Even for the perfect infinite structures, we study
50
51 supercavity modes by detuning parameters from its ideal BIC conditions. In particular, tuning of
52
53 incident angle scans the wave vector of the modes in a periodic structure by selecting the leaky
54
55 mode with different Q factors. Only for discrete values of incident angle, we observe a divergence
56
57
58
59
60
61
62
63
64
65

of Q factor due to BIC [24]. The resonance-trapped BICs in metasurfaces are less sensitive to the light direction because they are formed due to the local resonances, which can be excited by different plane waves and therefore they are related to flat bands on a band diagram [26]. In addition, the resonance-trapped BICs are affected by the geometrical parameters, in contrast to the symmetry protected BICs which does not depend on the structural geometry. In addition, the inevitable structural imperfectness due to the fabrication process could also break the spatial symmetry of the metasurface and convert perfect BICs into supercavity modes with a finite Q factor [45, 46].

Structure design. We consider a design of periodic dielectric metasurface that supports *resonance-trapped BICs*. The building block of the metasurface is a silicon cuboid with width W , length L and height H , as shown in **Figure 1**. The cuboids are arranged on a quartz substrate at the nodes of a square lattice with the lattice constant A . Such metasurfaces can be manufactured by a wide range of fabrication techniques, and at different size scales because of their striped air-groove structure. High-index dielectric antennas are known to possess a rich family of resonances [4-8], even when they are made of silicon [47]. The working principle of our active all-dielectric device is schematically illustrated in Figure 1a, where the supercavity modes are excited by the terahertz radiation and are modulated by the external optical pump stimulus.

Since the resonance-trapped BICs are sensitive to geometric sizes, we start the analysis by calculating the transmission spectra by tuning the length L of cuboid resonators while keeping other parameters unchanged. The eigenmodes analysis was performed by using commercial finite-element solver COMSOL Multiphysics where the metasurface array was built without considering the effect of substrate (cuboids suspended in air).

As shown in **Figure 2a**, all resonances show red-shift as the length of silicon resonators increase from 60 μm to 300 μm . At certain lengths, the sharp mode indicated by dashed black line demonstrates a vanishing nature, as shown in Figure 2a and the inset of Figure 2b. In addition, the Q factor of these sharp modes tends to diverge which is a common attribute of BICs [29, 36, 37], as shown in Figure 2b. We observe two BIC regions that are labeled as BIC I at 0.58 THz with $L = 165 \mu\text{m}$ and BIC II at 0.39 THz with L approaching 300 μm . It is worth noticing that the BICs in photonic crystal membranes are robust against the structural changes that preserve the spatial symmetry [45]. However, the scenario is different in the proposed metasurfaces. In the present case, the varying length of the cuboid L preserves the spatial symmetry (C_{2v}) but the BIC I transitions into a high- Q mode, which confirms the difference between the symmetry-protected and resonance-trapped BIC.

The BIC I gets suppressed due to the existence of substrate in the fabricated device with significant Rayleigh diffraction (i.e. appearance or disappearance of diffracted orders into evanescent modes). We therefore focus our study on BIC II mode by adopting rigorous coupled-wave analysis (RCWA). Using this method, it is convenient to introduce an operator of normal component of the wave-vector \hat{K}_z , whose eigenstates are evanescent and propagating modes lie in the normal direction by considering the periodic media to be an infinite continuation of the metasurface. RCWA yields amplitudes of the periodic media eigenstates as a function of frequency. In the metasurface with the length L below 300 μm and $W = 210 \mu\text{m}$, the supercavity mode is explained by the destructive interference between a propagating mode and an evanescent solution with imaginary K_z (see Supplementary Information). The analysis of eigenmode amplitudes makes it possible to evaluate Q factor directly (Figure 2b), because in the vicinity of resonance mode the amplitudes are described by the Lorentz function, in contrast to the transmission spectra with Fano

resonances as the result of the mode interference. The BIC mode manifests itself in the transmission spectra as a pronounced Fano resonance, which has an asymmetric line shape [48-50]. We extracted the resonance Q factors from the transmission spectra by using the Fano formula,

given by $T_{Fano} = \left| a_1 + ia_2 + \frac{b}{\omega - \omega_0 + i\gamma} \right|^2$, where a_1 , a_2 and b are constant real numbers; ω_0 is the

central resonant frequency; γ is the overall damping rate of the resonance. The experimental Q -factor was then determined by $Q = \omega_0/2\gamma$ [19, 50], which show similar results.

The wavevector (k_x) dependent transmission spectra (left panel) and band diagram (right panel) of the structure with $L = 270 \mu\text{m}$ and $W = 210 \mu\text{m}$ are plotted in Figure 2c. The band structure is calculated using the finite element method in COMSOL Multiphysics (red solid lines) and the results are reliably reproduced by using the Jacobi-Davidson method from CST microwave studio (red dots). By comparing the two panels in Figure 2c, the angle-resolved transmission spectra show consistent behavior of eigenmodes in the band structure, where the existence of eigenmodes imply that the THz wave can propagate and transmit through the periodic membrane. The resonance frequency and linewidth of the supercavity mode at 0.41 THz (in the vicinity of BIC II) are less sensitive to the symmetry-breaking perturbations near the Γ point (highlighted by the circles) but depend strongly on the cavity geometry. Therefore, we verify that the proposed system supports *resonance-trapped BICs*. Figure 2d shows the distributions of the electric and magnetic field in the cavity at the Γ point of the band highlighted by the circles. The magnetic field distribution exhibits a pair of magnetic dipoles along the z -axis oscillating out of phase. We note that unlike spherical or cylindrical dielectric resonators, a rigorous classification of modes of a dielectric cuboid do not exist [5-7]. Following the notation of ref. [6] one can use TE_{211}^z nomenclature to describe the observed modes in cuboids. Thus, we restrict ourselves to mode description in Figure 2d and leave cuboid mode classification beyond the scope of this work.

Experimental observation of THz supercavity modes. The samples were fabricated using high-resistivity silicon ($>10000 \Omega \cdot \text{cm}$) due to its low loss and low dispersion at THz frequencies. The designed schematic of all-dielectric metamaterials and the scanning electron microscope (SEM) images of fabricated sample are shown in Figure 1. Each individual resonator has a width of $W = 210 \mu\text{m}$ in the x -direction, length of $L = 270 \mu\text{m}$ in the y -direction, and height of $H = 200 \mu\text{m}$. The relatively large size of resonators operating in the THz band requires a different fabrication method from those operating in the visible and IR spectra [51]. In particular, such a thick silicon layer on insulator (SOI) could not be grown by chemical vapor deposition (CVD) and thus, it would be virtually impossible to fabricate these resonators by a conventional one-step reactive ion etching (RIE). Here, we followed a three-step fabrication procedure: (1) patterning of photoresist spin-coated silicon wafer with UV photolithography; (2) gluing the silicon wafer to a quartz substrate with UV curable adhesive (NOA 85, $n = 1.48$); (3) etching of silicon-on-quartz composite with deep reactive ion etching (DRIE) process (see Methods for details).

Figure 3a shows the theoretical transmission spectra by varying the resonator length from $230 \mu\text{m}$ to $270 \mu\text{m}$ with step size of $10 \mu\text{m}$, while the width $W = 210 \mu\text{m}$ is kept unchanged. Measured THz refractive indices of silicon ($n = 3.48$, see Supplementary Information) and quartz substrate ($n_{sub} = 2.14$, see Supplementary Information) were used to perform the numerical simulations. Overall, the resonances show red-shift and the Q factors increase as the resonator length increases. A non-zero (i, j) Rayleigh diffraction channel opens up at the frequency evaluated by $f = \frac{c}{\Lambda n_{sub}} \sqrt{i^2 + j^2}$, where c is vacuum light speed, Λ is the lattice constant, n_{sub} is refractive index of quartz substrate. Additional scattering channels result in decrease of Q factor and appears as a suppressed feature in the zero-order transmission spectra [52]. In our devices, this feature is observed at 0.47 THz (first order diffraction, $i = \pm 1, j = 0$), as shown in Figure 3a as a dashed black line. We restrict

our attention towards the low-frequency resonances below 0.47 THz for $L \geq 215 \mu\text{m}$ since they have relatively larger amplitude for identification and accurate measurement. To experimentally probe the high- Q resonance in the supercavity, we fabricated samples with the identical parameters as used in numerical calculations. The transmission spectra of each sample were measured using a continuous-wave (cw) THz spectroscopy (TeraScan 1550) with high spectral resolution for high- Q resonance measurements (see Methods for details). As shown in Figure 3b, the measured spectra show excellent agreement with the numerical calculations. The supercavity resonance mode below 0.47 THz reveals red-shift, and the corresponding Q factors gradually increase from 42 to 250 when L increases from 230 μm to 270 μm . The diffraction channel is also clearly observed at 0.47 THz indicated by a dashed black line as shown in Figure 3b, above which the transmission amplitude gets suppressed. We note that the accurate frequencies of diffraction kinks in the experiments reveal slight deviation due to the non-uniform thicknesses of UV curable adhesive in the samples.

A full map of transmission spectra by changing the length of the resonator from 60 μm to 300 μm is shown in Figure 3c. We observe the suppression of zero-order transmission mode above the frequency of non-zero diffraction channel at 0.47 THz as shown by the horizontal dashed black line. Therefore, the BIC I region disappears due to the excitation of high-order diffraction modes in samples with quartz substrate. The supercavity resonances reappear when the resonator length exceeds 215 μm , as illustrated in Figure 3c (vertical black dashed line). Above a specific resonator geometry, the numerically calculated and the experimentally measured supercavity resonances are plotted as red solid line and magenta dots in Figure 3c, respectively. Following the resonance evolution trajectory, we extracted the Q factors of numerical calculations (ideal case with air cladding, and real case with quartz substrate) and measured spectra, as plotted in Figure 3d. Overall,

1
2
3
4 the measured resonance Q factors show good agreement with the numerical simulations. The Q
5
6 factors for ideal case is significantly larger than that of real case. The maximum measured Q factor
7
8 is 250 which is the highest report value for THz dielectric metasurfaces. This also indicates the
9
10 transition from BIC to supercavity mode due to the existence of substrate that introduces an
11
12 asymmetric mode profile (additional scattering losses) within the structure. It should be noted that
13
14 the Q factor diverges for both ideal and real devices as the length of the silicon resonators
15
16 approaches 300 μm , which provides further evidence of the existence of resonance-trapped BICs.
17
18
19
20

21
22 **Active control of supercavity modes.** As one of the most promising applications, active
23
24 modulator with on-demand optical properties is a key technology in wave-front engineering, near-
25
26 field control of electromagnetic radiation, and multi-channel optical data processing [53]. In the
27
28 THz regime, optical pump and terahertz probe (OPTP) technique has been widely adopted to
29
30 investigate active THz metadevices [30-34]. Typically, these devices consist of an active layer
31
32 made of semiconductor such as Si, Ge, or GaAs, in addition to a metal-based resonator array. In
33
34 our device, the silicon cuboids act as the active medium due to photo-generated charge carriers
35
36 when pumped by an external optical stimulus with photon energy (1.55 eV) larger than the bandgap
37
38 of silicon (1.1 eV). The optically induced free carriers enable the change of conductivity on the
39
40 surface of silicon resonators with a penetration depth of about 10 μm [54]. Following the OPTP
41
42 approach (see Methods), we have experimentally demonstrated an active modulation of the THz
43
44 supercavity mode (sample with length of 230 μm , $Q = 42.36$) where the modulation depth is
45
46 controlled by applying a femtosecond pulsed laser stimulus (@800 nm wavelength, 1 KHz
47
48 repetition, 100 fs pulse width). As shown in **Figure 4a**, the supercavity mode is continuously
49
50 modulated in terms of resonance intensity as well as Q factor by gradually tuning the
51
52 photoexcitation pump fluence. The resonance peak (at 0.46 THz) as well as the two resonance dips
53
54
55
56
57
58
59
60
61
62
63
64
65

(at 0.43 THz and 0.53 THz) are completely switched off rendering a flat spectral response at an optical pump fluence of $63.5 \mu\text{J}/\text{cm}^2$ (power of 50 mW). During this modulation process, two interesting events appear (a) the resonance peak of the supercavity mode at 0.46 THz gradually diminishes and eventually quenches at a very low pump fluence of $10.16 \mu\text{J}/\text{cm}^2$ (average power of 8 mW), and (b) the broadband (0.3-0.6 THz) terahertz transmission spectrum becomes flat quenching the low quality factor modes as the pump fluence becomes larger than $10.16 \mu\text{J}/\text{cm}^2$. Upon photo-excitation, the strong damping due to the photo-induced free charge carriers prohibits the tight confinement of resonant field inside the silicon resonators. As the pump fluence is further increased, large number of photo-carriers dominantly damps and broadens the Mie resonance modes. Therefore, the resonant transmission dips (at 0.43 THz and 0.53 THz) gradually increase and disappear as a flat spectrum beyond pump fluence of $63.5 \mu\text{J}/\text{cm}^2$. In short, the two-stage modulation process occurs due to the change in the concentration of excited photo-carriers with the increase in pump fluence. First, the ultrasensitive supercavity mode damps out due to the optically excited photocarriers leading to the broadening of the resonance linewidth. The damping of the high- Q supercavity mode occurs at extremely low fluence of $10.16 \mu\text{J}/\text{cm}^2$, at which the loss is large enough to completely quench the strongly resonant mode. Further, the release of supercavity resonant energy leads to the overall increase of transmission amplitude at pump fluence larger than $10.16 \mu\text{J}/\text{cm}^2$.

The two-stage modulation of spectra can also be observed from the measured THz time-domain signals. Since photons are tightly confined inside the resonators at the supercavity mode without dominant loss channel, the oscillations in the THz time-domain pulse lasts longer than 100 ps as observed in Figure 4b. Once a loss channel is introduced, the oscillation amplitude of supercavity mode rapidly damps and thus ringing amplitude at longer time duration reduces significantly. The

contrast is clearly captured by introducing the pump stimulus (pump fluence of $63.5 \mu\text{J}/\text{cm}^2$) as shown in the inset plot of Figure 4b, where a rapid decay of oscillation occurs within 10 ps due to the excitation of large density of photocarriers. The evolution of time-domain pulses versus pump fluence is visualized clearly within 20 ps in Figure 4b. We have divided the time-domain pulse into two regions with gray and cyan background with a boundary at a time instant of 4 ps. The gradual amplitude damping in the gray region accounts for the modulation of supercavity mode intensity and Q factor, and the resonance mode (resonance peak at around 0.46 THz) vanishes at a fluence of $10.16 \mu\text{J}/\text{cm}^2$. On the other hand, the release of confined photons from the supercavity mode leads to the restoration of energy back into the main THz pulse as shown in the cyan region, where we observe the increase in amplitude of time-domain pulse as the pump fluence increases. This accounts for the gradual increase of broadband transmission amplitude at larger pump fluences in frequency domain as shown in Figure 4a.

In addition to the fluence dependent supercavity mode evolution, the transient dynamics reveal the time-resolved evolution of the supercavity mode. Since the modulation stems from generated photocarriers, we probed the dynamics of charge carriers in intrinsic silicon with the optical pump fluence of $63.5 \mu\text{J}/\text{cm}^2$ as shown in **Figure 5a**. Here, the differential transmission $-\Delta T/T_0$ is directly proportional to density of photocarriers, where $\Delta T = T(t) - T_0$, and $T(t)$ is the time-domain transmission amplitude through the sample at a given transient (t), and T_0 is the steady state amplitude (blue triangle in Figure 4b) of the sample in the absence of optical excitation. The transient $-\Delta T/T_0$ spectrum shows the carrier dynamics between the valence and conduction bands under optical pump, whose relaxation dynamics can be fitted by a single exponential decay function. The fitting equation is $-\Delta T/T_0 = A_0 + A_1 e^{-(t-t_0)/\tau}$, where A_0 and A_1 are constants, t_0 corresponds to the time when $-\Delta T/T_0$ reaches the maximum, and τ is the decay constant. Most of

1
2
3
4 carriers lie in valence band (VB) before the arrival of the pump pulses. Conduction band (CB) has
5
6 few residual carriers due to thermal effect from the laser pulse (repetition rate of 1 kHz). The
7
8 differential transmission ($-\Delta T/T_0$) dramatically increases within 12.68 ps due to the large amount
9
10 of photocarriers pumped into CB. The photocarriers cause the modulation of transmission
11
12 amplitude and thus the supercavity resonance spectrum, which is completely switched off at 12.68
13
14 ps as shown by the red curve in Figure 5b. The photocarriers gradually recombine following an
15
16 exponential decay with increasing time delay. In order to probe the transient evolution of the
17
18 supercavity mode, we present the measured transmission spectra at different temporal instants
19
20 (0.995, 1.662, and 2.596 ns) in Figure 5b, where we clearly observe the gradual recovery of the
21
22 supercavity mode in 2.6 ns to the original state. Thus, we consider 2.6 ns as the recovery time of
23
24 the metadvice, which enables a sub-gigahertz switching speed (see Supplementary Information
25
26 for more data). This switching speed could be further improved by several approaches, such as by
27
28 adopting ion-implanted silicon, direct band-gap semiconductors (GaAs), and/or intra-band effects
29
30 in semiconductors [30, 55, 56].
31
32
33
34
35
36
37
38

39 In summary, we have experimentally demonstrated an active control of all-dielectric THz
40
41 metasurfaces that support high- Q supercavity resonance mode in the vicinity of the *bound states*
42
43 *in the continuum* (BICs). Two BIC regions emerge by tailoring the geometrical length of the silicon
44
45 resonators, which are shown as the *resonance-trapped BICs*. Further, the dynamic switching and
46
47 modulation of the all-dielectric metadvice were shown at extremely low fluence of pump light.
48
49 In addition, a temporal spectral evolution of the supercavity resonance show sub-gigahertz
50
51 switching speed of the active metadvice. Our findings open a novel avenue for an active control
52
53 of all-dielectric BIC based metasurfaces that would enable design of active THz on-chip, ultrafast,
54
55 low-loss components and devices such as efficient modulators, filters, and biosensors. The simple
56
57
58
59
60
61
62
63
64
65

device architecture presented here would also provide a new route for designing scalable nanodevices for applications in low threshold nanolasers, on-chip parametric amplifiers, and higher harmonic generators.

METHODS

Numerical simulations. Numerical simulations were carried out by using commercial finite-element frequency-domain solver COMSOL Multiphysics for the case with normal incident plane wave and polarization along the x -axis (axis of resonator's width). The periodic boundary conditions were applied along the x/y -directions. A perfectly matching layer was used at the input and output ports.

Sample fabrication. $1.5 \mu\text{m SiO}_2$ is deposited on the high-resistivity silicon ($>10000 \Omega \cdot \text{cm}$) wafer with thickness of $200 \mu\text{m}$ by the plasma-enhanced chemical vapor deposition (PECVD), where the selectivity of the etching gas ions on Si and SiO_2 determines the deposition thickness of the SiO_2 layer. The hybrid silicon dioxide-on-silicon wafer is patterned by conventional UV photolithography on SiO_2 with a $1.5 \mu\text{m}$ layer of AZ5214E photoresist. Silicon dioxide-on-silicon wafer with patterned photoresist is then directly bonded to a quartz (1 mm, Z-cut) substrate with a thin layer of spin-coated UV curable polymer optical adhesive (Norland Optical Adhesive 85) and exposed to UV light (2.5 W/cm^2) for 10 mins. After bonding, the SiO_2 layer is removed by mixed gases of CHF_3 and CF_4 and the remaining pattern is kept as a protection mask for subsequent etching. The silicon wafer is etched by the DRIE (deep reactive-ion etching technique; Oxford Estrelas). Each cycle of the Bosch process consists of sidewall passivation (C_4F_8) and etching (SF_6) steps. Each cycle of the Bosch process consists of deposition for 5 s and etching for 15 s. In the deposition step, the C_4F_8 gas (85 sccm) is utilized with 600 W ICP power at 35 mTorr pressure. During the etching step, a mixture of SF_6 (130 sccm) and O_2 (13 sccm) is applied with 600 W ICP

power and 30 W bias power, at 35 mTorr pressure. This process cycle is then repeated until the silicon is completely removed. Solid silicon micro-cube arrays are kept attached to the quartz substrate. The periodicities in x and y directions are both 300 μm .

Terahertz frequency-domain spectroscopy measurements. The measurements were performed using commercially available terahertz system (TeraScan 1550 from Toptica). It is a continuous wave-based THz spectroscopy system with high frequency resolution, which has combined coherent generation and detection of THz radiation in frequency-domain using fiber coupled photoconductive antennas (InGaAs PCAs). Two distributed feedback (DFB) lasers at adjacent frequencies illuminate the photo mixer antennas to generate THz radiation and detect THz signal by measuring the photocurrent at the detector PCA [57]. To resolve the spectral feature of the sample, the frequency was swept from 0.3 THz to 0.6 THz in 10 MHz step size with 100 ms integration time. The measurements were done at room temperature and in the dry nitrogen atmosphere to nullify the effect due to water vapor absorption.

Optical pump-THz probe (OFTP) spectroscopy. Passive transmission and dynamic performance of the all-dielectric metamaterials were performed using the optical pump-THz probe (OFTP) spectroscopy setup. A near-infrared laser beam (Ti: sapphire oscillating laser system, 35 fs, 6 mJ per pulse at 800 nm with 1 kHz repetition rate) was coherently split into three parts: external pump source, pump beam for generation of terahertz radiation and detection beam for THz detection. To capture the active modulation of THz transmission, the transmitted THz time-domain signal through the samples were recorded with a scan length of 100 ps. The first echo signal can be delayed by increasing the thickness of substrate, which allows longer scan length of the main terahertz signal. In experiments, the samples on 1 mm quartz were attached to an identical 10 mm thick quartz substrate to delay the first echo by ~157 ps. As a result, the time-domain

1
2
3
4 system shows frequency resolution around ~ 6.37 GHz, which is suitable for measuring resonance
5
6 with Q -factor smaller than 63 at around 0.40 THz (sample with $L = 230$ μm and $W = 210$ μm).
7
8 Further, the optical pump fluence is tuned by a neutral density filter to capture the modulated time-
9
10 domain signal. The time domain signals were transformed to frequency domain and normalized
11
12 by using an identical bare quartz substrate as the reference by $|\tilde{T}(\omega)| = |\tilde{E}_S(\omega)/\tilde{E}_R(\omega)|$, where
13
14 $\tilde{E}_S(\omega)$ and $\tilde{E}_R(\omega)$ are the spectra of sample and reference after Fourier transform, respectively.
15
16 For the measurements of free carrier dynamics, we set the synchronized position of THz probe and
17
18 optical pump at the maximum of time-domain THz pulse at the blue triangle as shown in Figure
19
20
21
22
23
24 4b and monitored the time-varied THz amplitude at this point by changing the pump delay time.
25
26
27

28 **Supporting Information**

29 Supporting Information is available from the Wiley Online Library or from the author.
30
31
32

33 **Acknowledgements**

34 The authors (S.H., L.Q.C., Y.K.S., A.K., W.X.L., and R.S.) acknowledge Singapore Ministry of
35 Education (MOE), Grants MOE2011-T3-1-005, and MOE2015-T2-2-103. M.V.R. and Y.S.K.
36 acknowledge support by the Ministry of Education and Science of the Russian Federation
37 (3.1500.2017/4.6) and the Australian Research Council. We acknowledge Mr. Jipeng Qi from
38 University of California, Berkeley for discussion of RCWA algorithm. We also thank Mr. Thomas
39 Tan Cai Wei and Mr. Piyush Agarwal for helping with the OPTP and CW THz measurements,
40
41 respectively.
42
43

44 Received: ((will be filled in by the editorial staff))

45 Revised: ((will be filled in by the editorial staff))

46 Published online: ((will be filled in by the editorial staff))
47
48

49 **References**

- 50
51
52 [1] R. D. Richtmyer, *J. Appl. Phys.* **1939**, 10, 391.
53
54 [2] J. C. Sethares, and S. J. Naumann, *IEEE Trans. Microw. Theory Tech.* **1966**, 14, 2.
55
56 [3] S. B. Cohn, *IEEE Trans. Microw. Theory Tech.* **1968**, 16, 218.
57
58 [4] S. Long, M. McAllister, and L. Shen, *IEEE Trans. Antennas Propag.* **1983**, 31, 406.
59
60
61
62
63
64
65

- 1
2
3
4 [5] D. Kajfez, and P. Guillon, "Dielectric resonators". Artech House: Norwood, MA, **1986**.
5
6 [6] R. K. Mongia, and P. Bhartia, *Int. J. RF Microw. Comput.-Aided Eng.*, **1994**, 4, 230.
7
8 [7] R. K. Mongia, and A. Ittipiboon, *IEEE Trans. Antennas Propag.* **1997**, 45, 1348.
9
10 [8] S. O'Brien, and J. B. Pendry, *Journal of Physics: Condensed Matter*, **2002**, 14, 4035.
11
12 [9] J. B. Pendry, A. J. Holden, D. J. Robbins, and W. J. Stewart, *IEEE Trans. Microw. Theory*
13
14
15
16
17
18
19
20
21
22 [10] Q. Zhao, J. Zhou, F. Zhang, and D. Lippens, *Mater. Today* **2009**, 12, 60.
23
24 [11] S. Jahani, and Z. Jacob, *Nat. Nanotech.* **2016**, 11, 23.
25
26 [12] A. I. Kuznetsov, A. E. Miroshnichenko, M. L. Brongersma, Y. S. Kivshar, and B.
27
28
29
30
31
32
33
34
35
36
37
38
39
40
41
42
43
44
45
46
47
48
49
50
51
52
53
54
55
56
57
58
59
60
61
62
63
64
65
- [13] I. Staude, and J. Schilling, *Nat. Photon.* **2017**, 11, 274.
- [14] P. Genevet, F. Capasso, F. Aieta, M. Khorasaninejad, and R. Devlin, *Optica* **2017**, 4, 139.
- [15] M. Khorasaninejad, and F. Capasso, *Science* **2017**, 358, eaam8100.
- [16] S. Kruk, and Y. Kivshar, *ACS Photonics* **2017**, 4, 2638.
- [17] D. G. Baranov, D. A. Zuev, S. I. Lepeshov, O. V. Kotov, A. E. Krasnok, A. B. Evlyukhin,
and B. N. Chichkov, *Optica* **2017**, 4, 814.
- [18] S. M. Kamali, E. Arbabi, A. Arbabi, and A. Faraon, *Nanophotonics* **2018**, 7, 1041.
- [19] Y. Yang, I. I. Kravchenko, D. P. Briggs, and J. Valentine, *Nat. Commun.* **2014**, 5, 5753.
- [20] C. Wu, N. Arju, G. Kelp, J. A. Fan, J. Dominguez, E. Gonzales, E. Tutuc, I. Brener, and
G. Shvets, *Nat. Commun.* **2014**, 5, 3892.
- [21] A. E. Miroshnichenko, A. B. Evlyukhin, Y. F. Yu, R. M. Bakker, A. Chipouline, A. I.
Kuznetsov, B. Luk'yanchuk, B. N. Chichkov, and Y. S. Kivshar, *Nat. Commun.* **2015**, 6,
8069.

- 1
2
3
4 [22] Y. Yang, W. Wang, A. Boulesbaa, I. I. Kravchenko, D. P. Briggs, A. Puretzky, D.
5
6 Geohegan, and J. Valentine, *Nano Lett.* **2015**, 15, 7388.
7
8
9 [23] Y. Shen, V. Rinnerbauer, I. Wang, V. Stelmakh, J. D. Joannopoulos, and M. Soljacic, *ACS*
10
11 *Photonics* **2015**, 2, 27.
12
13 [24] C. W. Hsu, B. Zhen, J. Lee, S. L. Chua, S. G. Johnson, J. D. Joannopoulos, and M. Soljačić,
14
15 *Nature* **2013**, 499, 188.
16
17 [25] C.W. Hsu, B. Zhen, A. D. Stone, J. D. Joannopoulos, and M. Soljačić, *Nature Review*
18
19 *Materials* **2016**, 1, 16048.
20
21 [26] A. Kodigala, T. Lepetit, Q. Gu, B. Bahari, Y. Fainman, and B. Kanté, *Nature* **2017**, 541,
22
23 196.
24
25 [27] M. Rybin, and Y. K. Kivshar, *Nature* **2017**, 541, 164.
26
27 [28] A. Tittl, A. Leitis, M. Liu, F. Yesilkoy, D. Y. Choi, D. N. Neshev, Y. S. Kivshar, and H.
28
29 Altug, *Science* **2018**, 360, 1105.
30
31 [29] M. V. Rybin, K. L. Koshelev, Z. F. Sadrieva, K. B. Samusev, A. A. Bogdanov, M. F.
32
33 Limonov, and Y. S. Kivshar, *Phys. Rev. Lett.* **2017**, 119, 243901.
34
35 [30] M. R. Shcherbakov, S. Liu, V. V. Zubyuk, A. Vaskin, P. P. Vabishchevich, G. Keeler, T.
36
37 Pertsch, T. V. Dolgova, I. Staude, I. Brener, and A. A. Fedyanin, *Nat. Commun.* **2017**, 8,
38
39 17.
40
41 [31] S. V. Makarov, A. S. Zalogina, M. Tajik, D. A. Zuev, M. V. Rybin, A. A. Kuchmizhak, S.
42
43 Juodkasis, and Y. S. Kivshar, *Laser and Photonics Rev.* **2017**, 11, 1700108.
44
45 [32] J. Gu, R. Singh, X. Liu, X. Zhang, Y. Ma, S. Zhang, S. A. Maier, Z. Tian, A. K. Azad, H.
46
47 T. Chen, and A. J. Taylor, *Nat. Commun.* **2012**, 3, 1151.
48
49
50
51
52
53
54
55
56
57
58
59
60
61
62
63
64
65

- 1
2
3
4 [33] S. Zhang, J. Zhou, Y. S. Park, J. Rho, R. Singh, S. Nam, A. K. Azad, H. T. Chen, X. Yin,
5
6 A. J. Taylor, and X. Zhang, *Nat. Commun.* **2012**, 3, 942.
7
8
9 [34] M. Manjappa, Y. K. Srivastava, L. Cong, I. Al-Naib, and R. Singh, *Adv. Mater.* **2017**, 29,
10
11 1603355.
12
13
14 [35] K. Sakoda, *Phys. Rev. B* **1995**, 52, 7982.
15
16 [36] D. C. Marinica, A. G. Borisov, and S. V. Shabanov, *Phys. Rev. Lett.* **2008**, 100, 183902.
17
18 [37] C. Blanchard, J. P. Hugonin, and C. Sauvan, *Phys. Rev. B* **2016**, 94, 155303.
19
20 [38] X. Gao, C. W. Hsu, B. Zhen, X. Lin, J. D. Joannopoulos, M. Soljačić, and H. Chen, *Sci.*
21
22 *Rep.* **2016**, 6, 31908.
23
24
25 [39] Y. Yang, C. Peng, Y. Liang, Z. Li, and S. Noda, *Phys. Rev. Lett.* **2014**, 113, 037401.
26
27
28 [40] B. Zhen, C. W. Hsu, L. Lu, A. D. Stone, and M. Soljačić, *Phys. Rev. Lett.* **2014**, 113,
29
30 257401.
31
32
33 [41] A. Krasnok, and A. Alú, *J. Opt.* **2018**, 20, 064002.
34
35
36 [42] F. Monticone, H. M. Doeleman, W. Den Hollander, A. F. Koenderink, and A. Alù, *Laser*
37
38 *and Photonics Rev.* **2018**, 12, 1700220.
39
40
41 [43] M.V. Rybin, D. S. Filonov, K. B. Samusev, P. A. Belov, Y. S. Kivshar, and M. F. Limonov,
42
43 *Nat. Commun.* **2015**, 6, 10102.
44
45
46 [44] S. V. Li, Y. S. Kivshar, and M. V. Rybin. *ACS Photonics* **2018**, 5, 4751.
47
48 [45] S. P. Shipman, and S. Venakides, *Phys. Rev. E* **2005**, 71, 026611.
49
50
51 [46] L. Yuan, and Y. Y. Lu, *Opt. Lett.* **2017**, 42, 4490.
52
53 [47] D. Hou, W. Hong, W. L. Goh, J. Chen, Y. Z. Xiong, S. Hu, and M. Madihian, *IEEE*
54
55 *Antennas Propag. Mag.* **2014**, 56, 80.
56
57
58 [48] H. Friedrich, and D. Wintgen, *Phys. Rev. A* **1985**, 32, 3231.
59
60
61
62
63
64
65

- 1
2
3
4 [49] A. N. Poddubny, M. V. Rybin, M. F. Limonov, and Y. S. Kivshar, *Nat. Commun.* **2012**, 3,
5
6 914.
7
8
9 [50] M. F. Limonov, M. V. Rybin, A. N. Poddubny, Y. S. Kivshar, *Nat. Photon.* **2017**, 11, 543.
10
11 [51] Z. Ma, S. M. Hanham, P. Albella, B. Ng, H. T. Lu, Y. Gong, S. A. Maier, and M. Hong,
12
13 *ACS Photonics* **2016**, 3, 1010.
14
15 [52] N. A. Gippius, S. G. Tikhodeev, and T. Ishihara, *Phys. Rev. B* **2005**, 72, 045138.
16
17 [53] N. I. Zheludev, and E. Plum, *Nat. Nanotechnol.* **2016**, 11, 16.
18
19 [54] I. Al-Naib, G. Sharma, M. M. Dignam, H. Hafez, A. Ibrahim, D. G. Cooke, T. Ozaki, and
20
21 R. Morandotti, *Phys. Rev. B* **2013**, 88, 195203.
22
23 [55] V. I. Klimov, C. J. Schwarz, D. W. McBranch, and C. W. White, *Appl. Phys. Lett.* **1998**,
24
25 73, 2603.
26
27 [56] Y. Yang, K. Kelley, E. Sacht, S. Campione, T. S. Luk, J. P. Maria, M. B. Sinclair, and I.
28
29 Brener, *Nat. Photon.* **2017**, 11, 390.
30
31 [57] A. J. Deninger, A. Roggenbuck, S. Schindler, and S. Preu, *J. Infrared Milli. Terahz. Waves*
32
33 **2015**, 36, 269.
34
35
36
37
38
39
40
41
42
43
44
45
46
47
48
49
50
51
52
53
54
55
56
57
58
59
60
61
62
63
64
65

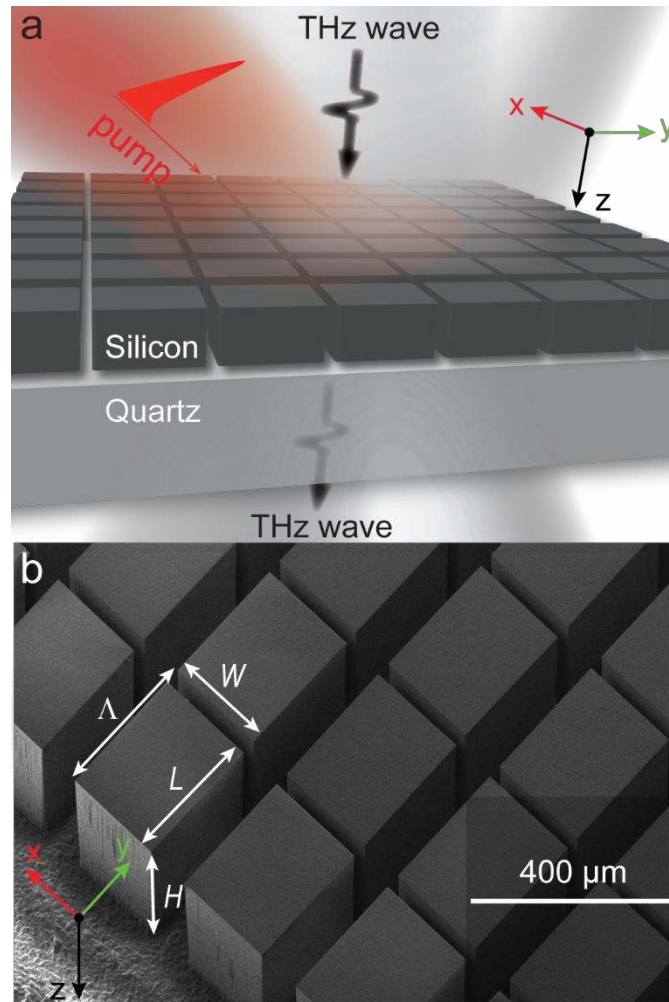


Figure 1. Design of active all-dielectric BIC driven metadvice. (a) Schematic view of the all-dielectric metamaterial. The properties of the dielectric resonators are actively modulated by applying an external optical pump. (b) Perspective view of the fabricated sample by scanning electron microscope. The geometrical parameters are lattice constant $\Lambda = 300 \mu\text{m}$, length $L = 270 \mu\text{m}$ (along y axis), width $W = 210 \mu\text{m}$ (along x axis), and height $H = 200 \mu\text{m}$.

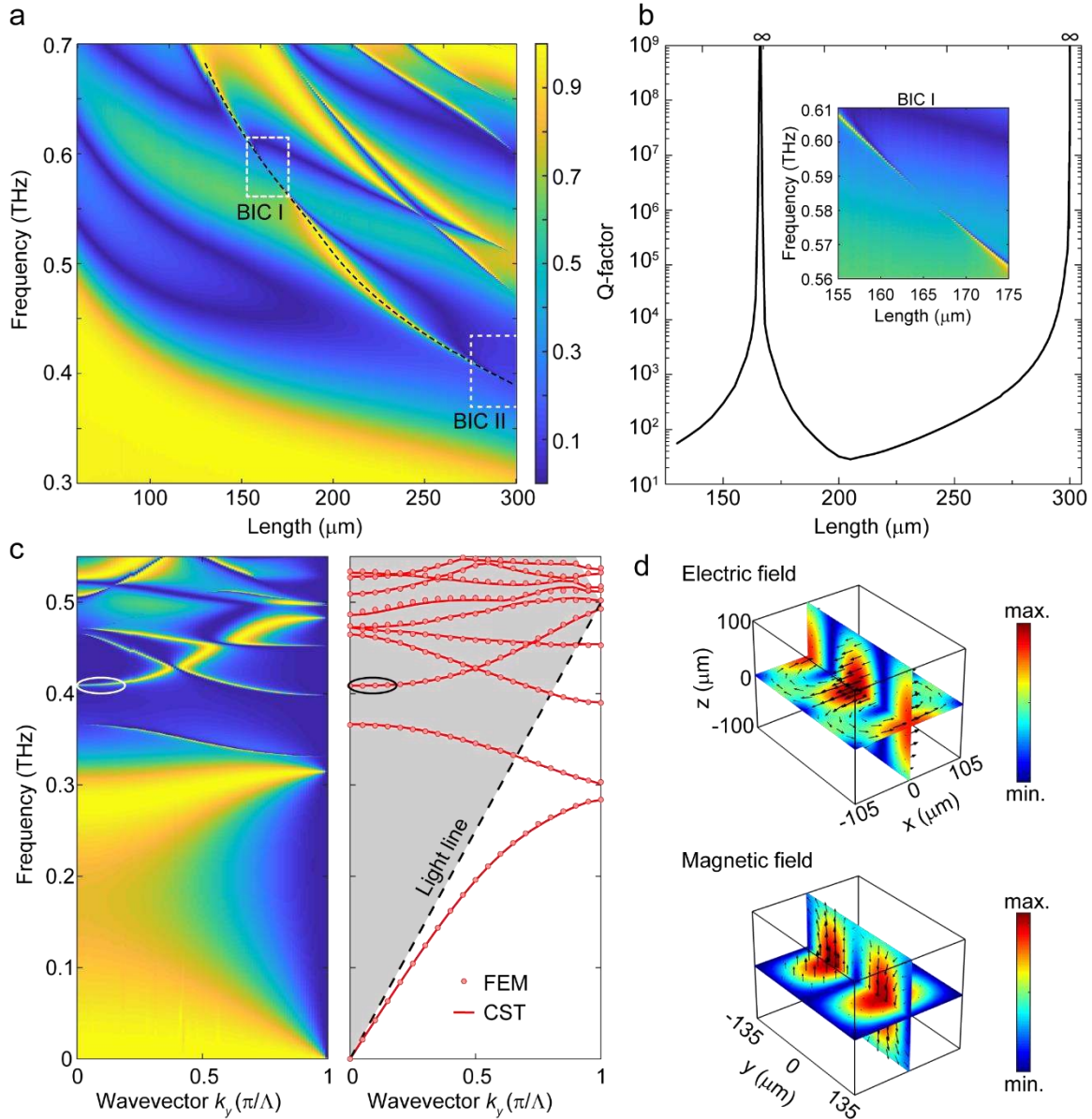


Figure 2. Bound states in the continuum and supercavity resonance. (a) Map of transmission spectra by sweeping the cuboid length from 60 μm to 300 μm , where the width (210 μm) and the height (200 μm) are kept constant. The THz wave impinges at normal incidence. The low frequency mode is marked by black dashed curve. Two BIC regions are indicated on the selected low frequency mode. (b) Evolution of Q factor at the low frequency mode of the metasurface by changing the cuboid length. Inset: the disappearance of transmission mode at BIC I at $L = 165 \mu\text{m}$.

1
2
3
4 (c) Angle-resolved transmission spectra (left panel) and band diagram (right panel) of the silicon
5 resonator in square lattice. The band structures calculated by COMSOL Multiphysics (red line)
6 reliably reproduces the one obtained by the CST microwave studio (dots). (d) The corresponding
7 electric and magnetic field profile for the TE-like eigenmodes at the Γ -point with frequency of
8
9
10
11
12
13
14 0.41 THz. The incident wave is polarized along x axis in (a) and (b). The light line in (c) is labelled
15
16
17
18
19
20
21
22
23
24
25
26
27
28
29
30
31
32
33
34
35
36
37
38
39
40
41
42
43
44
45
46
47
48
49
50
51
52
53
54
55
56
57
58
59
60
61
62
63
64
65

as dashed black line.

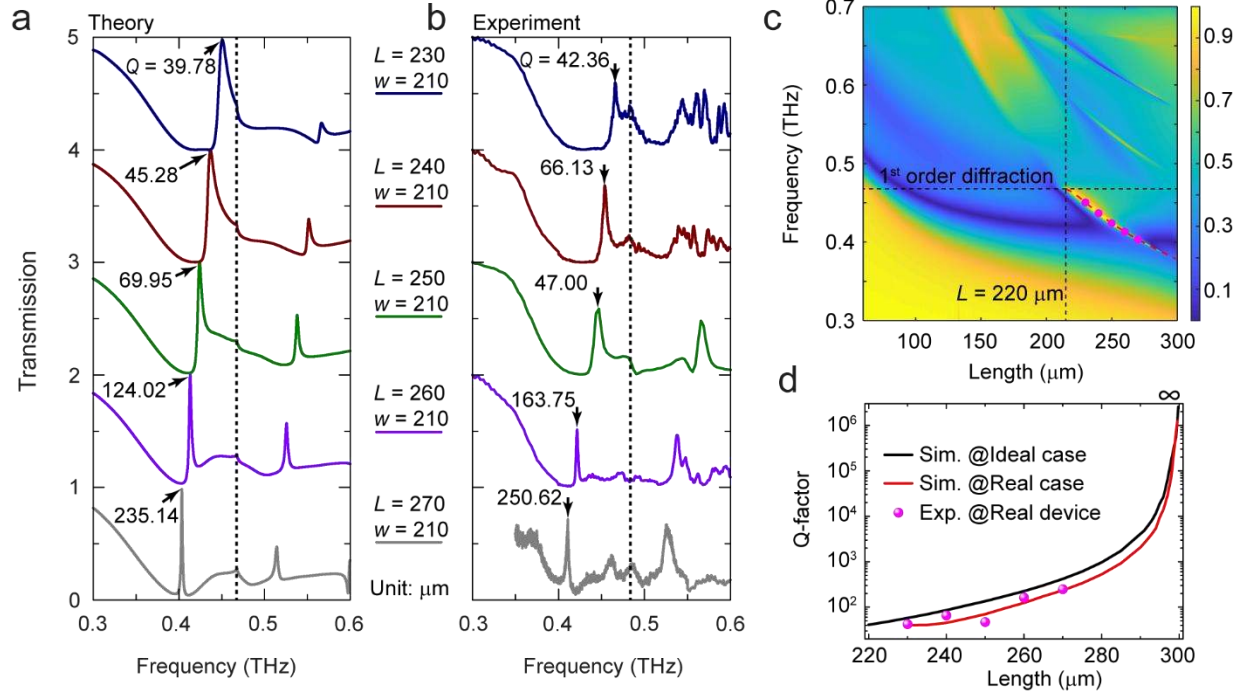


Figure 3. Experimental measurement of the high- Q supercavity mode in all-dielectric metadvice. (a) Transmission spectra of the proposed device at normal incidence by changing length of the cuboid resonator L from 230 μm to 270 μm with a step size of 10 μm in numerical calculations. The dashed line indicates the frequency where the first order diffraction occurs. (b) Corresponding transmission spectra from measurements with the same parameters as simulations. (c) The map of numerical transmission spectra for real devices by changing the resonator length L . The horizontal dashed line indicates the emergence of the first order diffraction, and the vertical dashed line indicates the geometric length where the supercavity mode emerges. (d) Comparison of Q factors for the ideal case with air cladding (black curve), real case with quartz substrate (red curve), and experimentally captured Q factors from measurements (magenta dots).

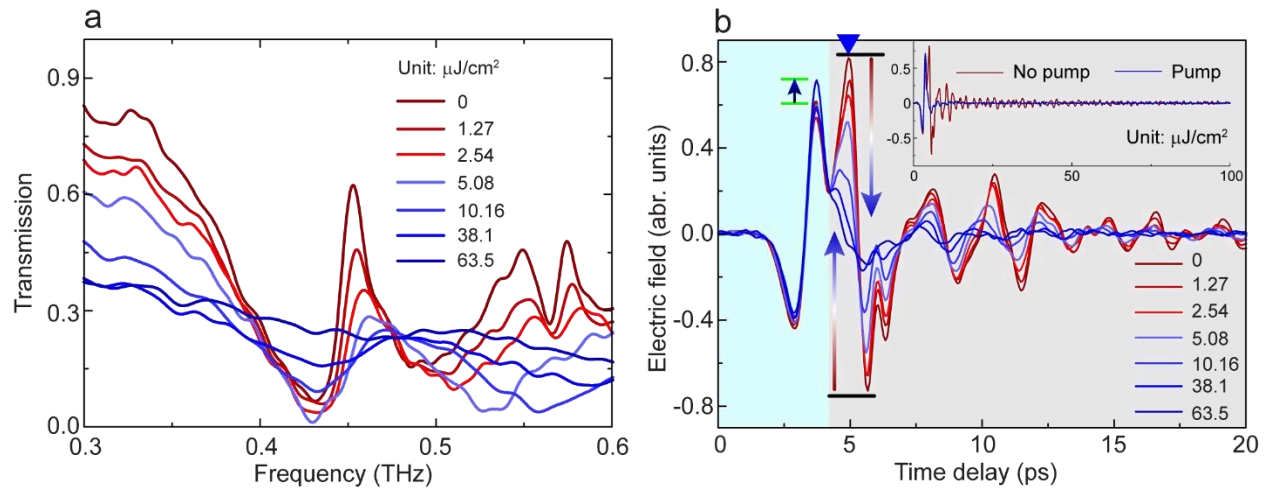


Figure 4. Photoexcitation dependent dynamic modulation of the supercavity resonance. (a) Experimentally measured transmission spectra showing the continuous modulation of supercavity mode by tuning the pump fluence. **(b)** Corresponding time-domain pulse modulation by varying pump fluence within 20 ps. Two regions are indicated to explain the fluence dependent mode evolution behaviors. Inset: Full length of time-domain pulses for 100 ps with and without optical pump.

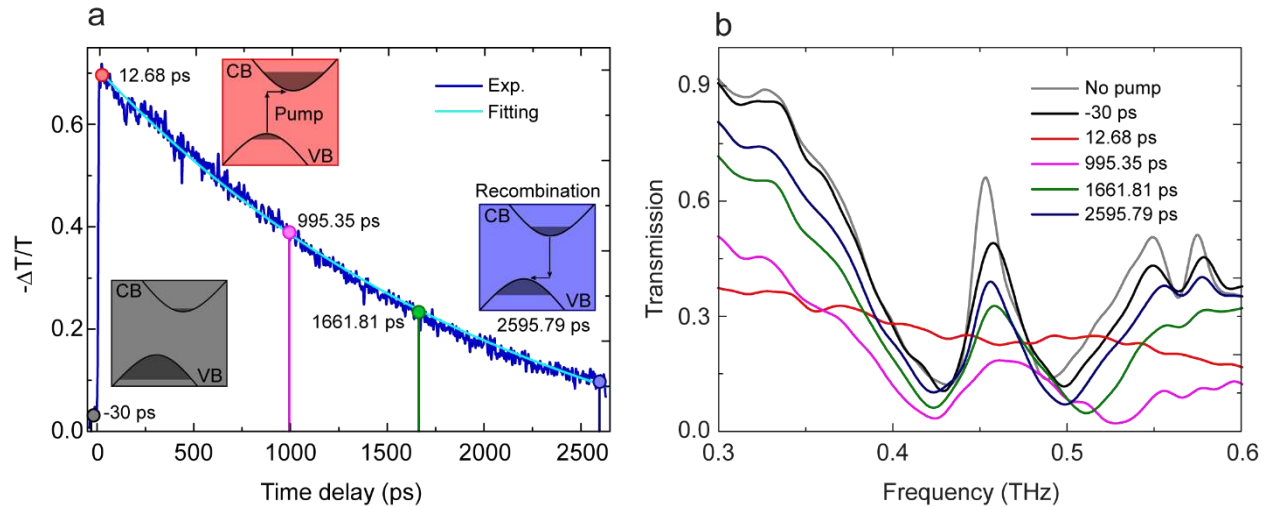


Figure 5. Temporal evolution of the supercavity resonance. (a) Measured differential transmission of THz time-domain amplitude at 4.8 ps (blue triangle in Figure 4b) as a function of delay time of pump pulse. The relaxation dynamics is scanned for 2650 ps with a femtosecond pump pulse (@800 nm, 1.55 eV, silicon band gap ~ 1.14 eV). The cyan curve is the exponential fitting of the carrier-relaxation. Insets show the schematic illustration of carrier concentration at various time delays. (b) Measured transient frequency-domain transmission spectra of the supercavity device at various time delays.

The table of contents entry should be 50–60 words long, and the first phrase should be bold.
The entry should be written in the present tense and impersonal style.

Keyword ((Terahertz; All-dielectric metasurface; Bound states in the continuum; Optically active metadevices))

*Song Han^{1,2}, Longqing Cong^{1,2}, Yogesh Kumar Srivastava^{1,2}, Bo Qiang^{2,3}, Mikhail V. Rybin^{4,5},
 Abhishek Kumar^{1,2}, Ravikumar Jain⁶, Wen Xiang Lim^{1,2}, Venu Gopal Achanta⁶, Shriganesh S.
 Prabhu⁶, Qijie Wang^{2,3}, Yuri S. Kivshar^{5,7}, and Ranjan Singh^{1,2*}*

Song Han, Dr. Longqing Cong, Dr. Yogesh Kumar Srivastava, Abhishek Kumar, Dr. Wen Xiang Lim, and Prof. Ranjan Singh
 Division of Physics and Applied Physics, School of Physical and Mathematical Sciences,
 Nanyang Technological University, Singapore 637371, Singapore

Song Han, Dr. Longqing Cong, Dr. Yogesh Kumar Srivastava, Bo Qiang, Abhishek Kumar, Dr. Wen Xiang Lim, Prof. Qijie Wang, and Prof. Ranjan Singh
 Centre for Disruptive Photonic Technologies, The Photonics Institute,
 Nanyang Technological University, Singapore 639798, Singapore
 E-mail: ranjans@ntu.edu.sg

Bo Qiang and Prof. Qijie Wang
 Centre for OptoElectronics and Biophotonics, School of Electrical and Electronic Engineering
 and The Photonics Institute, Nanyang Technological University, Singapore 639798, Singapore

Dr. Mikhail V. Rybin
 Ioffe Institute, St Petersburg 194021, Russia

Dr. Mikhail V. Rybin and Prof. Yuri S. Kivshar
 ITMO University, St Petersburg 197101, Russia

Prof. Yuri S. Kivshar
 Nonlinear Physics Center, Australian National University, Canberra ACT 2601, Australia

Ravikumar Jain, Prof. Venu Gopal Achanta, and Prof. Shriganesh S. Prabhu
 Department of Condensed Matter Physics and Material Science, Tata Institute of Fundamental
 Research, Mumbai 400005, India

All-dielectric active photonics driven by bound states in the continuum

ToC figure ((Please choose one size: 55 mm broad × 50 mm high **or** 110 mm broad × 20 mm high.
 Please do not use any other dimensions))

((Supporting Information can be included here using this template))

Copyright WILEY-VCH Verlag GmbH and Co. KGaA, 69469 Weinheim, Germany, 2016.

Supporting Information

All-dielectric active photonics driven by bound states in the continuum

*Song Han^{1, 2}, Longqing Cong^{1, 2}, Yogesh Kumar Srivastava^{1, 2}, Bo Qiang^{2, 3}, Mikhail V. Rybin^{4, 5},
Abhishek Kumar^{1, 2}, Ravikumar Jain⁶, Wen Xiang Lim^{1, 2}, Venu Gopal Achanta⁶, Shriganesh S.
Prabhu⁶, Qijie Wang^{2, 3}, Yuri S. Kivshar^{5, 7}, and Ranjan Singh^{1, 2*}*

1. Fano fitting for Q -factor extraction

We used a Fano model to extract the Q -factor of the sharp resonance from the dielectric metamaterials [58]. The numerically simulated and experimentally measured transmission spectra were fitted to a Fano line shape given by $T_{Fano} = \left| a_1 + ia_2 + \frac{b}{\omega - \omega_0 + i\gamma} \right|^2$, where a_1 , a_2 and b are constant real numbers; ω_0 is the central resonant frequency; γ is the overall damping rate of the resonance. The experimental Q -factor was then determined by $Q = \omega_0/2\gamma$. Two fittings (simulation and experiment) for the sample with geometric parameters of length $L = 250 \mu\text{m}$ and width $W = 210 \mu\text{m}$ are shown in **Figure S1**. The fitting parameters for all samples are summarized in Table 1 and Table 2 as shown below.

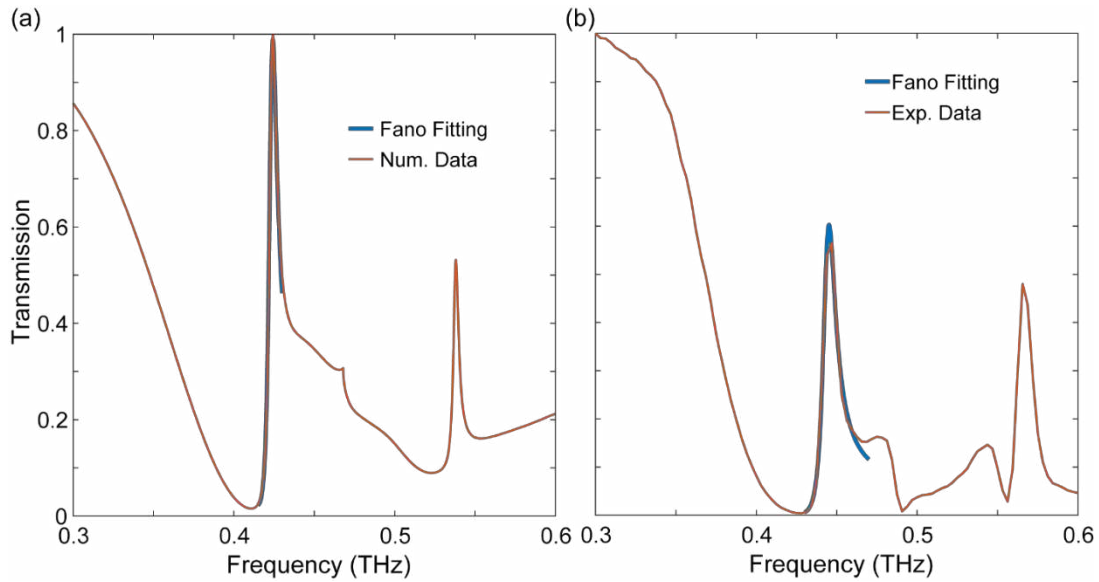


Figure S1. Fano fittings. (a) Numerically calculated and (b) the experimentally measured transmission for the sample with geometric parameters of length $L = 250 \mu\text{m}$ and width $W = 210 \mu\text{m}$.

Supplementary Table 1. Fitting parameters for the numerical transmissions

Fano Parameters	$L = 230$ $W = 210$	$L = 240$ $W = 210$	$L = 250$ $W = 210$	$L = 260$ $W = 210$	$L = 270$ $W = 210$
a_1	0.3595	0.3614	0.2549	0.1192	-0.01156
a_2	0.1538	0.1547	0.2333	0.2219	0.1815
b	0.0056	0.0048	0.00345	0.002	0.00101
$\gamma/(2*\pi)$ in THz	0.00563	0.0048	0.00302	0.00167	8.58E-4
$\omega_0/(2*\pi)$ in THz	0.4482	0.4349	0.4232	0.413	0.4035
Q-factor	39.77636	45.28322	69.95041	124.02402	235.13986

Supplementary Table 2. Fitting parameters for the experimentally measured transmissions

Fano Parameters	$L = 230$ $W = 210$	$L = 240$ $W = 210$	$L = 250$ $W = 210$	$L = 260$ $W = 210$	$L = 270$ $W = 210$
a_1	0.1724	0.1326	0.1824	0.06444	-0.20327
a_2	0.1092	0.1225	0.1128	0.1057	0.2097
b	0.00456	0.00312	0.00396	0.00106	8.30709E-4
$\gamma/(2*\pi)$ in THz	0.00548	0.00343	0.00472	0.00129	8.202E-4
$\omega_0/(2*\pi)$ in THz	0.4643	0.4531	0.4439	0.4215	0.4111
Q-factor	42.35541	66.12668	47.00339	163.75291	250.6190

2. Rigorous coupled wave analysis

The rigorous coupled wave analysis (RCWA) is widely used for calculations of the scattering and propagation of waves through periodic photonic crystal membranes [P. Lalanne and G. M. Morris J. Opt. Soc. Am. A, 13 779 (1996); D. M. Whittaker, I. S. Culshaw PRB 60, 2610 (1999); S. G. Tikhodeev et al. PRB 66, 045102 (2002)]. The periodicity allows us to expand solution as a function of x and y into 2D Fourier series. Next, the space is divided by three parts: the substrate, the metasurface and the air, which are homogeneous along z axis. The eigenmodes in the substrate and in the air can be expressed analytically. The modes in the periodic metasurface are found numerically by solving an eigenvalue problem for K_z (the z component of wave vector). The

amplitudes of incident waves are given as initial conditions and the amplitudes of the outgoing waves (including evanescent ones) are found from the Maxwell's boundary conditions similar as the scattering and transfer matrix techniques.

The RCWA uncovers physics of the supercavity mode under consideration. **Figure S2** demonstrates that the supercavity mode is generated by two contributions. The first one is the propagation wave with real wave vector $k_z \approx \pm 113 \text{ cm}^{-1}$ and the second one is a pair of evanescent waves with imaginary wave vectors $k_z \approx i \cdot 148 \text{ cm}^{-1}$ and $k_z \approx i \cdot 189 \text{ cm}^{-1}$. The amplitudes of these waves are well described by the Lorentz functions with similar width. A transmission vanishing at interfaces is known to arise due to the destructive interference outside. Thus, in our case the modes inside the metasurface are almost uncoupled from the free space owing to their destructive interference outside. Similar mechanism was described by Friedrich and Wintgen for states in quantum systems [59].

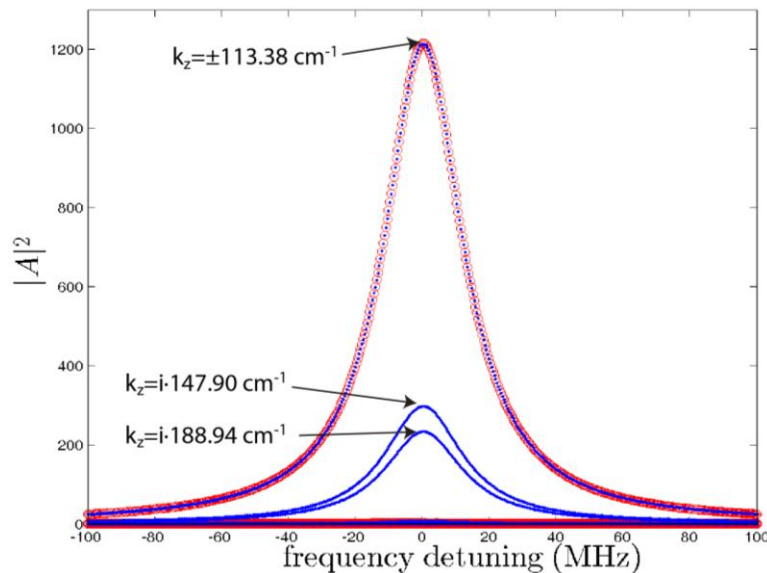


Figure S2. Supercavity mode analysis by RCWA. Spectra of $|A|^2$ of waves with positive (negative) real part of Kz is shown by blue (red) symbols. $L=295 \mu\text{m}$, $W=210 \mu\text{m}$, $H=200 \mu\text{m}$, $P=300 \mu\text{m}$. Polarization along x axis. Central frequency $f=0.390856 \text{ THz}$.

To demonstrate that the resonance-trapped BIC is less sensitive to the angle of incidence, we compare Q factor of different modes in the same geometry $L=166.83 \mu\text{m}$ and $W=210 \mu\text{m}$ with the RCWA method (see **Figure S3**). The first mode corresponds to symmetry-protected BIC at 0.538 THz and the second mode corresponds to resonance-trapped BIC (labeled BIC I in the manuscript). At the normal incidence both modes become BIC with infinite Q factors. The changing of the incidence angle leads to finite Q factors for both modes, while the Q factor of the mode related to the BIC I decrease slowly. At the 5° , the difference between Q factors is an order of magnitude.

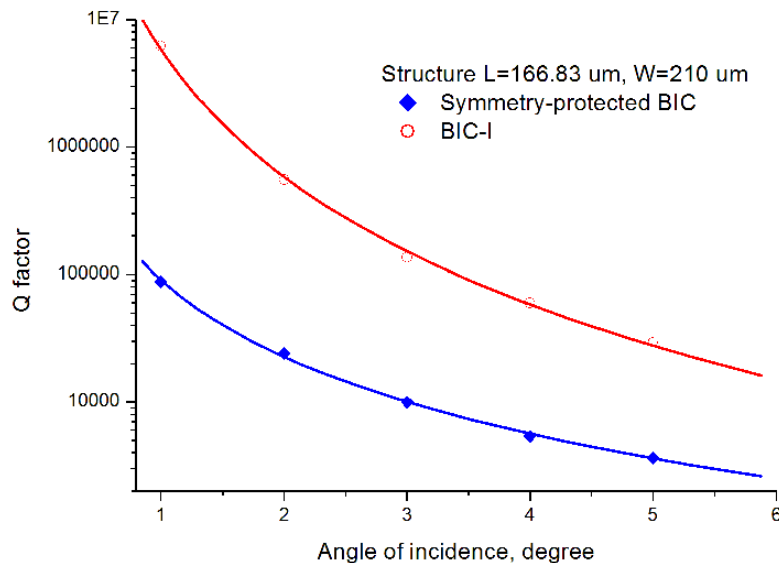


Figure S3. Q factor of mode related to *symmetry-protected BIC* (blue) and *resonance-trapped BIC* (red) as a function of incidence angle.

3. Optimization of geometric parameters

To clearly show the dependence of the supercavity modes on different geometry parameters, we discuss the simulated data below.

a) Effect of W on BIC

To quantify the effect of width on BIC, we performed extensive numerical simulation by varying the width of resonators, where the length is fixed at $270\ \mu\text{m}$ and the height is fixed at $210\ \mu\text{m}$. The transmission maps are shown in **Figure S4(a)** without substrate and **S4(b)** with quartz as substrate.

From these two maps, we can conclude:

- i. The supercavity mode shifts to the lower frequency as the width of resonator increases.
- ii. The linewidth of the supercavity mode (i.e. Q factor of resonance) does not change with width (W) of the structure.
- iii. To avoid the non-zero Rayleigh diffraction (radiation losses at $0.47\ \text{THz}$ due to periodic quartz substrate), the width of structure should be larger than $130\ \mu\text{m}$, as shown in **Figure R3(b)**. Therefore, the chosen width ($W = 210\ \mu\text{m}$) of our structure ensures that supercavity mode is not suppressed by the Rayleigh diffraction. This guarantees that the supercavity modes can be experimentally measured.

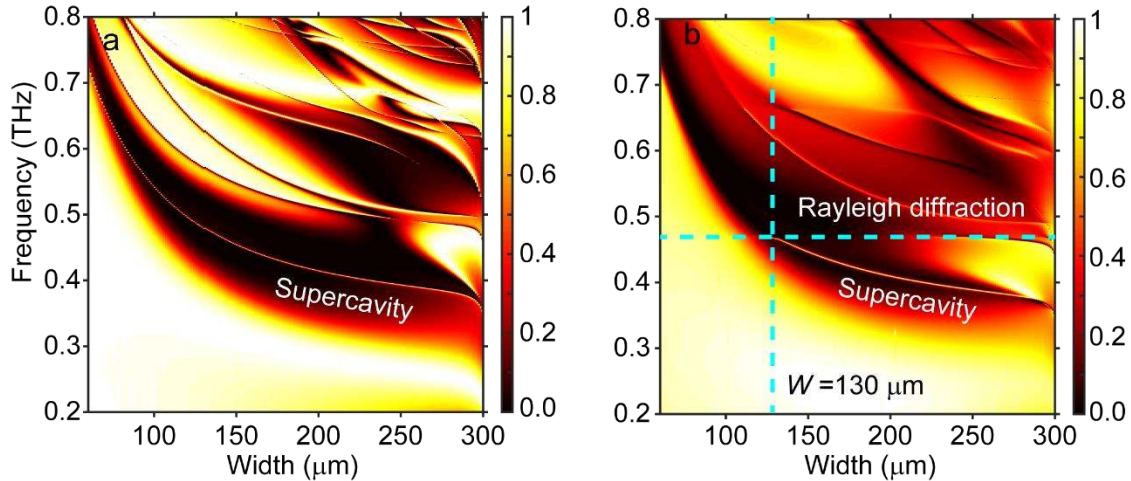


Figure S4. The color map of transmission spectra by changing the resonator height H , while the length and width are kept constant at $270\ \mu\text{m}$ and $210\ \mu\text{m}$, respectively. The dashed cyan line labels the 1st order diffraction where the supercavity mode shows at $H = 60\ \mu\text{m}$. (a) air cladding and (b) quartz as substrate (real sample scenario).

b) Effect of H on BIC

The height-dependent transmission map is shown in **Figure R4**. The simulation results suggest:

- i. The supercavity mode shifts to the lower frequency as the height of resonator increases.
- ii. The linewidth of supercavity mode does not dramatically change as the height of resonator increases.
- iii. The 1st order diffraction lies at $0.47\ \text{THz}$ once quartz is taken as substrate, as shown in **Figure R4(b)**. Therefore, the resonator's height should be larger than $60\ \mu\text{m}$ to avoid the suppression of supercavity mode. The selected geometric parameter with a height of $200\ \mu\text{m}$ is optimized for ease of fabrication and measurements.

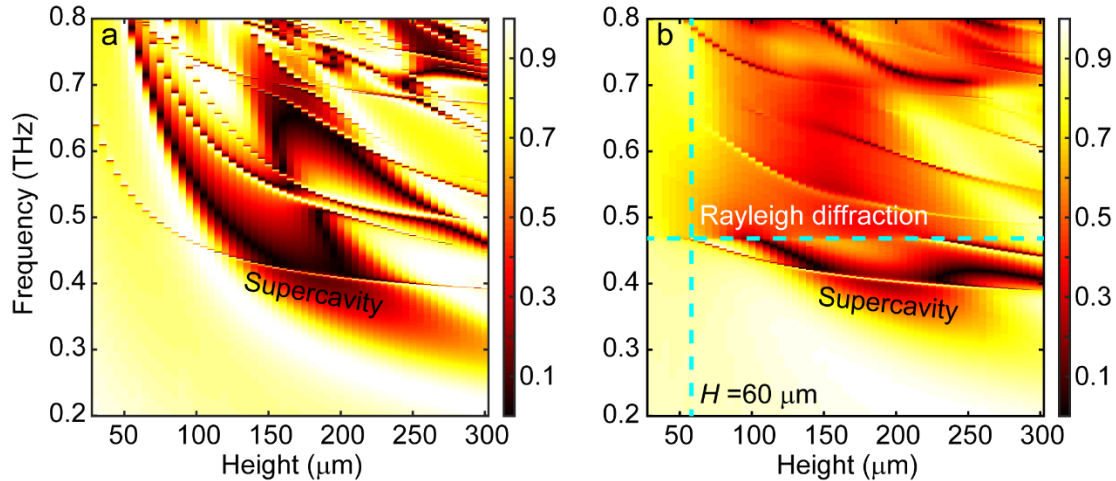


Figure S5. The color map of transmission spectra by changing the resonator height H , while the length and width are kept as $270\ \mu\text{m}$ and $210\ \mu\text{m}$ unchanged. The dashed cyan line labels the 1st order diffraction where the supercavity mode shows at $H = 60\ \mu\text{m}$. (a) air cladding and (b) quartz as substrate.

In conclusion, the linewidth of resonances, or Q factor, are not obviously dependent on the width (W) and height (H) of the resonators. Therefore, we restrict our discussion on the different geometric length (L) while keeping the width (W) and height (H) of the resonators unchanged. Particularly, the width ($W = 210\ \mu\text{m}$) and height ($H = 200\ \mu\text{m}$) are optimized to avoid the 1st order diffraction at frequency of BIC-II, and meanwhile guarantee the feasibility of fabrication and experiments of the samples. We have added these discussions to the Supplemental materials in the revised manuscript.

4. Experimental study of the materials' properties with THz-TDS

We measured the refractive indexes of silicon and quartz by using a ZnTe-based THz-TDS. The transmitted time-domain THz pulse for 200- μm silicon (Orientation $\langle 100 \rangle$) and 1-mm quartz (z-cut) are plotted in **Figure S6**. Compared to the reference signal (THz pulse for dry nitrogen atmosphere), transmitted peak field decreases due to the materials' reflections at the interfaces and absorption in materials even though the absorption is small. Silicon has the largest refractive index among three, so it has lowest transmitted THz pulse with the fixed initial position. THz pulses of silicon and quartz are delayed respect to nitrogen. Quartz has the largest delay since the thickness is 5 times of silicon. The two materials under used are optically thick samples, which indicates the THz signal drops zero before echo comes out. With the time-domain pulses and accurate sample thicknesses, the refractive indices are calculated by solving $\tilde{T}(\omega) = \frac{2\tilde{n}(\tilde{n}_{sup} + \tilde{n}_{sub})}{(\tilde{n} + \tilde{n}_{sup})(\tilde{n} + \tilde{n}_{sub})} \cdot e^{(-i(\tilde{n} - \tilde{n}_{sub})\frac{\omega d}{c})} \cdot FP(\omega)$, where ω and c are the angular frequency and speed of light in a vacuum. The complex refractive index \tilde{n} is the one to be solved, and \tilde{T} is the complex transmission that is calculated by fast Fourier transform. $FP(\omega)$ is the frequency dependent contribution of Fabry-Perot reflections, and here it is one since silicon and quartz film are optically thick samples with thickness of d . The wafers are cladded by Nitrogen so the complex refractive indices \tilde{n}_{sup} and \tilde{n}_{sub} are taken as the refractive index of air. As shown in **Figure S6**, both silicon and quartz have negligible absorption in the frequency regime of interest. The refractive index of silicon and quartz are around $3.4773 + i \cdot 0.0145$ and $2.1356 + i \cdot 0.0027$, respectively, with negligible dispersion in the frequency range of interest. These experimentally extracted values are taken for numerical simulations and theoretical calculations in this article.

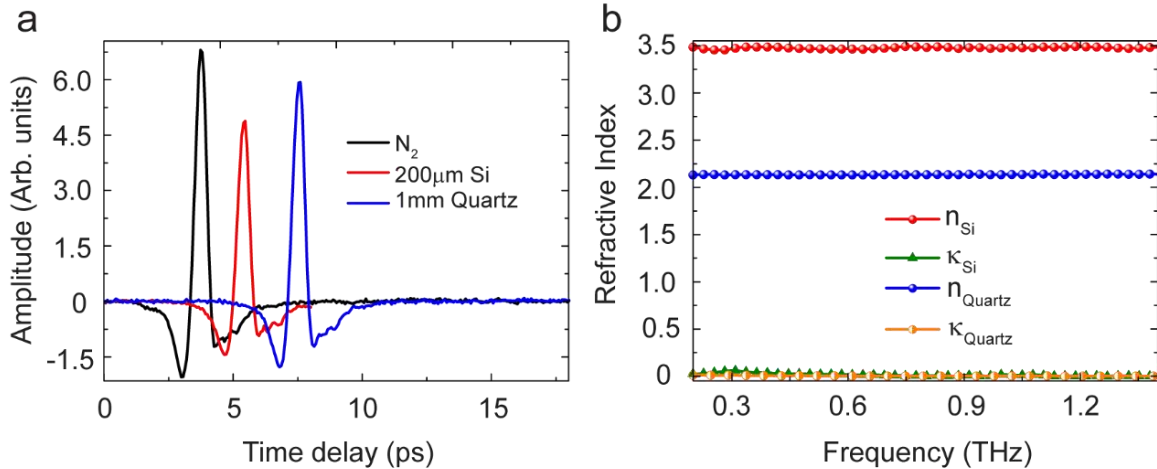


Figure S6. Experimental study the THz properties of 200 μm silicon (orientation $\langle 100 \rangle$) and 1 mm quartz (z-cut). (a) Transmitted time-domain THz pulses for dry nitrogen, silicon and quartz. (b) Corresponding refractive indexes for silicon and quartz with reference of nitrogen.

5. Transmission comparison between 200 μm silicon film and the proposed metadvice with pump

As reference, we measured the bared silicon film under same pump as the measurements for our fabricated sample, as shown in **Figure S7**. It is clearly shown that the transmitted THz is continuously reduced as pump power increasing. Then the transmission is almost zero as the pump power is 80 mW, which demonstrates the silicon film has been fully metalized under this pump power.

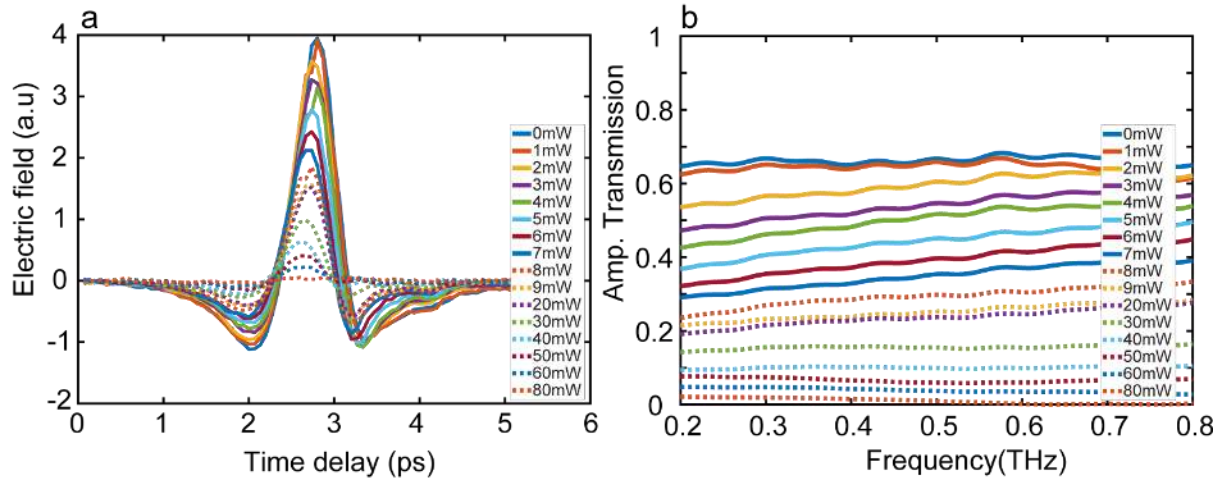


Figure S7. The time-domain pulses and transmission spectra of optically pump silicon film with thickness of 200 μm . (a) The time domain pulses are continuously weakened upon pump of 800 nm laser. The THz beam is totally blocked by the metallized silicon with pump power of 80 mW, i.e. fluence of 101.6 $\mu\text{J}/\text{cm}^2$. (b) The transmissions obtained from fast Furrier transform with reference of N_2 . They continuously decrease and close to zero as the pump power of 80 mW as well.

However, thing is different for the patterned silicon rectangular resonators array on quartz substrate. THz photons are tightly confined inside the resonators due to the existence of the high- Q mode in the silicon resonator so that they oscillate in the resonators for a long time, as shown in **Figure S8**. We observe a strong ringing (oscillations) in the THz time-domain pulse lasting for around 100 picoseconds for the passive (No pump) state of the metadvice. The strong damping of photo-excited carriers leads to a very fast decay of the oscillations under strong photo-excitation. As result, the ringing in the THz transmitted pulse decays rapidly. The decay time for largest pump is about 10 picoseconds, after which the transmitted signal is around zero. To clearly visualize the gradual modulation, we plot the time-domain pulse within 20 picoseconds, as shown in the inset of **Figure S8**. It is clearly observed that the strong oscillations of THz pulse after 4 picoseconds

gradually damps with different pump powers, and finally goes to zero with an external photoexcitation, verifying the continuous modulation of the supercavity mode. By using Fourier transform, the time domain signals are transformed into frequency domain spectra, as shown in **Figure S9**. The resonance continuously decreases upon optical pump and saturates around pump power of 8 mW ($10.16 \mu\text{J}/\text{cm}^2$ in main text). Then the transmission goes up overall as the pump power larger than 8 mW. The strong damping due to the photo-induced free charge carriers hinder the incoming THz to be tightly trapped inside the inside the silicon resonators. As a result, the resonance continuously decreases as the optical pump increasing. Then the supercavity mode is switched off around pump of 8 mW. Much more photo-carriers are injected to silicon so that the damping is larger enough for the resonators to dissipate even the Mie resonance as pump getting even stronger. Therefore, the transmission dips continuously raise and become a flat spectrum after all.

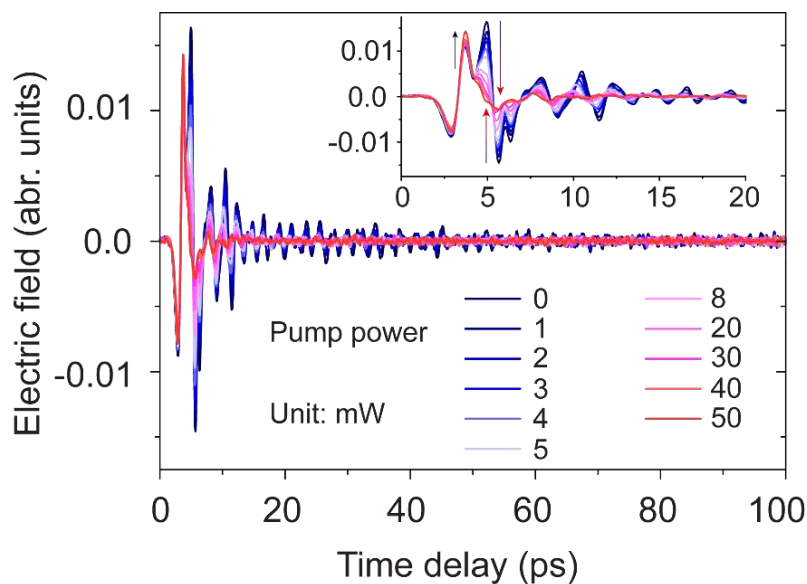


Figure S8. Terahertz time-domain pulses of optically pumped device. The full time-domain pulses were captured with a scan length of 100 picoseconds. The inset figure plots the truncated THz

time-domain pulses within 20 picoseconds. The continuous reduction of time-domain electric field after 4 picoseconds is indicated by two gradient arrows, while the enhancement of time-domain electric field before 4 picoseconds is indicated by a black arrow.

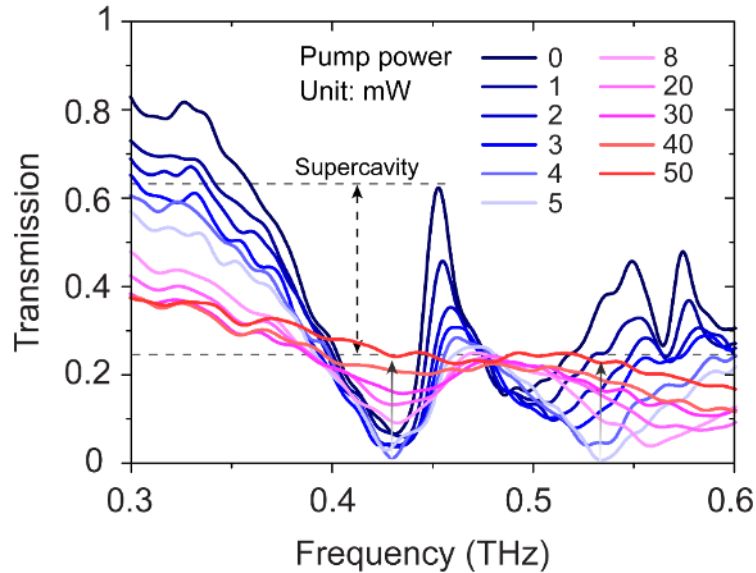


Figure S9. The transmission spectra of optically pumped device. The spectra demonstrate the continuously modulation of the device under different pump power. The supercavity mode (dashed double side arrow between two dashed gray lines) is much sensitive so it saturates at pump power of 8 mW. The broadband transmission dips (around 0.43 THz and 0.53 THz) show continuously enhancement (two gradient arrows) as the pump fluence becomes larger than $10.16 \mu\text{J}/\text{cm}^2$.

6. Exponential fitting of the negative differential transmission $-\Delta T/T_0$

Figure S10 shows the negative differential transmission $-\Delta T/T_0$ under different optical pump, where $\Delta T = T(t) - T_0$ is the absolute transmission change, $T(t)$ being the transmission of a THz wave through the sample at a given transient (t), and T_0 is the amplitude at the peak pulse

(maximum of the time-domain pulse in Supplementary Figure 4) for the sample in the absence of optical excitation. $-\Delta T/T_0$ evaluates the carrier dynamics between the valence and conduction bands under optical pump, which can be fitted by a single exponential decay equation. The fitting equation is $-\Delta T/T_0 = A_0 + A_1 e^{-(t-t_0)/\tau}$, where A_0 is a constant, and A_1 is the amplitude determining the weight of the exponential function, t_0 corresponds to the time at maximum value of $-\Delta T/T_0$, and τ is the decay time constant. The black curves present the fittings for different dynamics under different pump pulses. The delay time constants are summarized in Supplementary Table 3. It's obviously demonstrated that the relaxation time for our proposed silicon based metadvice is different under different pump powers. The relaxation becomes slow as the pump power getting stronger.

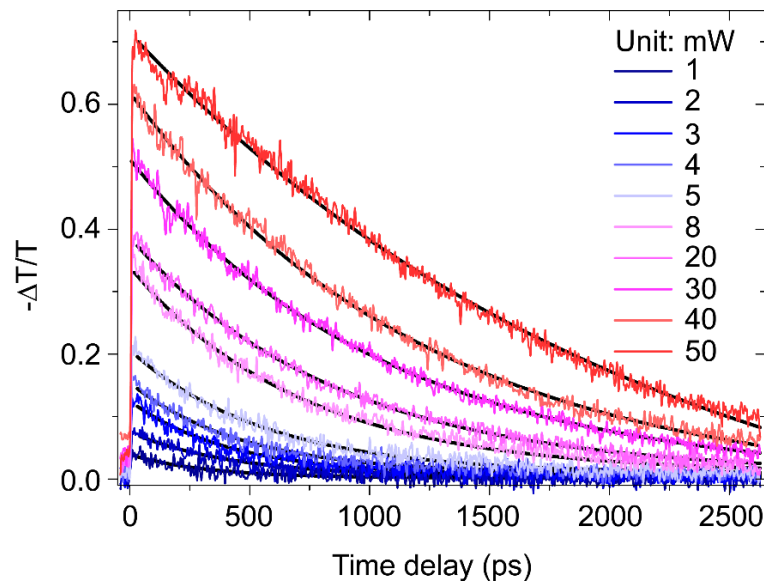


Figure S10. The dynamic evolution of optically pumped device under different pump power. The black curves demonstrate the exponential fitting for the dynamics.

Supplementary Table 3. Fitting of $-\Delta T/T_0$ for the decay time constant of silicon based metadvice under different pump powers

Pump Power (mW)	Relaxation time (τ) (ps)
1	328 ± 10
2	435 ± 8
3	422 ± 4
4	468 ± 3.7
5	565 ± 3.6
8	704 ± 3
20	855 ± 3
30	1066 ± 4
40	1219 ± 5
50	2182 ± 17

7. Point group analysis

Ref. [3] provides mode symmetry analysis of a square lattice (C_{4v} point group) showing that at the Γ point only the E modes couples to the external radiation field. Here we analyze modes of cuboids arranged in a square lattice having a lower symmetry C_{2v} , because the C_4 rotation does not retain the structural geometry in our case. The C_{2v} point group has 4 one-dimensional irreducible representations A_1, A_2, B_1, B_2 [60]. It is important that these representations do not relate to the A_1, A_2, B_1, B_2 representations of the C_{4v} group. The reduction procedure is used to yield the proper relationship between the representations of two types of point groups. The one-dimensional representations A_1, A_2, B_1, B_2 of the C_{4v} group become the representations A_1, A_2 of the C_{2v} group and the two-dimensional representation E is reduced to a pair of one-dimensional representations B_1, B_2 of the C_{2v} group. Thus, in our samples only the B_1, B_2 modes couple to the external radiation field, while A_1, A_2 modes have infinite lifetime as they from symmetry-protected BICs. The table S4 shows characters of the representations for the the C_{2v} group.

Let us consider the irreducible representations A_1, A_2 of the C_{2v} point group. For both of them the C_2 rotation changes signs of Cartesian components $(F_x; F_y)$ to $(-F_x; -F_y)$. Also the symmetry mirror reflection operation σ_x changes $(F_x; F_y)$ to $(F_x; -F_y)$ and σ_y changes $(F_x; F_y)$ to $(-F_x; F_y)$ for the A_1 representations. It means that the x component of the A_1 representation is an odd function of x and the y component of the A_1 representation is an odd function of y , simultaneously. It is straightforward to get the same relations for the A_2 representations. At the same time, a plane wave with $k_x=k_y=0$ (the Γ point) is constant along x and y . Therefore, the parity mismatch does not allow coupling of the A_1, A_2 modes with the freely radiating field and these representations correspond to the symmetry-protected BICs.

Supplementary Table 4. Character table for the C_{2v} point group. From [60].

C_{2v}	E	C_2	σ_x	σ_y
A_1	1	1	1	1
A_2	1	1	-1	-1
B_1	1	-1	1	-1
B_2	1	-1	-1	1

8. Analysis of BIC under study

The aim of this subsection is to demonstrate that the mode under the study is neither symmetry-protected BIC nor off- Γ BIC typical for photonic crystal slabs. The electromagnetic field distributions are shown in Fig. 2d. The electrodynamic problem can be fully defined either by electric or magnetic field and it is straightforward to prepare a table of the mode modification under the transformations from the C_{2v} point group.

C_{2v}	E	C_2	σ_x	σ_y	representation
Electric field	1	-1	-1	1	B_2
Magnetic field	1	-1	1	-1	B_1

Thus, if we consider the electric field the mode is a B_1 representation; if we consider the magnetic field the mode is a B_2 representation. At the same time the free space plane waves have the B_1 or B_2 representation as well. Thus, the symmetry does allow coupling between the modes and the free space and it is not a symmetry-protected BIC.

Now we consider the difference between the BICs shown in Fig. 2d and off- Γ BIC typical for photonic crystal slabs in the following table:

off- Γ BIC typical for photonic crystal slabs	BIC shown in Fig. 2d
Observed at off- Γ points	Observed at the Γ point.
Corresponds to ‘oblique’ branches with strong dispersion typical for photonic crystal slabs.	Corresponds to ‘flat’ branches with negligible dispersion typical for metasurfaces.
Robust against structural changes that preserve the spatial symmetry.	Transforms into high- Q supercavity modes with the variation of the structure parameters that preserve the spatial symmetry.

Also Figure S2 demonstrates that the BIC mode under the study is occurs due to the destructive interference between tails of leaky modes. Therefore, it is another type of BIC, which we call as *resonance-trapped BIC*.

Reference

- 1
2
3
4 [58] Y. Yang, et al. All-dielectric metasurface analogue of electromagnetically induced
5 transparency. Nat. Commun. 5, 5753 (2014).
6
7
8
9 [59] H. Friedrich, and D. Wintgen, Interfering resonances and bound states in the continuum.
10 Phys. Rev. A 32, 3231 (1985).
11
12
13 [60] K. Sakoda, Optical properties of photonic crystals. Vol. 80. Springer Science & Business
14 Media, 2004.
15
16
17
18
19
20
21
22
23
24
25
26
27
28
29
30
31
32
33
34
35
36
37
38
39
40
41
42
43
44
45
46
47
48
49
50
51
52
53
54
55
56
57
58
59
60
61
62
63
64
65



Click here to access/download
Production Data
Figure1.png



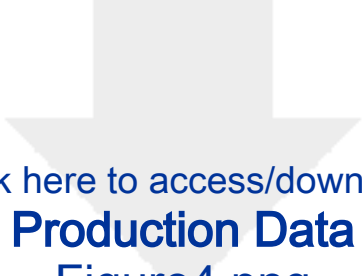
[Click here to access/download](#)

Production Data
Figure2.png

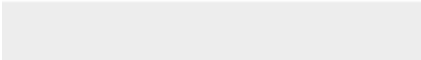


[Click here to access/download](#)

Production Data
Figure3.png



Click here to access/download
Production Data
Figure4.png





Click here to access/download
Production Data
Figure5.png

